PCCP

Accepted Manuscript

ROYAL SOCIETY OF CHEMISTRY

www.rsc.org/pccp

Remarkable changes in the photoluminescent properties of $Y_2Ce_2O_7:Eu^{3+}$ red phosphors through the modifications of cerium oxidation states and oxygen vacancy ordering

Athira K.V. Raj, P. Prabhakar Rao*, T.S. Sreena, S. Sameera, Vineetha James and U. A. Renju

Materials Science and Technology Division, CSIR-National Institute for Interdisciplinary Science and Technology (NIIST), Trivandrum – 695 019, India

Abstract

New series of Eu^{3+} doped yttrium cerate based red phosphors: $Y_{1.9}Ce_2O_7$:*0.1*Eu^{3+}, $Y_2Ce_{1.9}O_7$:*0.1*$Eu^{3+}$and $Y_2Ce_{2-x}O_7$:*x*Eu^{3+} (*x* = 0.05, 0.10, 0.15, 0.20, 0.25 and 0.50) were prepared via conventional solid state method. Influence of Eu^{3+} substitution at aliovalent site on the photoluminescent properties was elucidated using powder X-ray diffraction, FT-Raman, X-ray photoelectron spectroscopy, transmission electron microscope, scanning electron microscope with energy dispersive spectrometer, UV-visible absorption spectroscopy, photoluminescence and life time measurements. The Eu^{3+} substitution at Ce^{4+} site induces a structural transition from a defect fluorite to C-type structure which increases the oxygen vacancy ordering, distortion of Eu^{3+}environment and also decreases the formation of Ce^{3+} states. Whereas the isovalent substitution at Y^{3+} site exhibits biphasic nature of defect fluorite and C-type and thereby increases the Ce^{3+} oxidation states. These modifications made remarkable changes in the photoluminescent properties of $Y_2Ce_{1.9}O_7$:0.1Eu^{3+}red phosphors with emission intensities 3.8 times greater than that of the $Ce_{0.9}O_2$:0.1Eu^{3+} and $Y_{1.9}Ce_2O_7$:*0.1*Eu^{3+}. Thus the photoluminescent properties of $Y_2Ce_{2-x}O_7$:*x*Eu^{3+} was studied with different Eu^{3+} concentrations under blue excitation. These phosphors emit intense red light due to $^5D_0$-$^7F_2$ transition under 466nm excitation and no concentration quenching is observed upto 50 mol% of Eu^{3+}. They show increased life times with Eu^{3+} concentration in the range of 0.62-0.72ms. The cation ordering linked to the oxygen vacancy ordering led to the uniform distribution of Eu^{3+} ions in the lattice allowing higher doping concentrations

without quenching and consequently increasing the $^5D_0$ states life time. Our results demonstrate that significant improvements in the photoluminescence properties can be achieved by structural variation of fluorite CeO_2 to a C-type lattice.

Keywords: Red phosphor; Cerium oxide; Fluorite; C-type

---

* Corresponding author. Tel.: + 91 471 2515311; Fax: + 91 471 2491712

Email ID: padala_rao@yahoo.com (P. PrabhakarRao)

1. Introduction

In the last two decades, rare earth (RE) ion doped oxide phosphors have fascinated much attention due to their distinctive optical properties, such as long fluorescent lifetime, large Stokes shift and combination of high luminescence efficiency and good photochemical stability.[1, 2] These desirable characteristics make them potentially applicable in the industry fields of fluorescent lamps, biological labels, field emission displays and so on. The oxide phosphors possess higher chemical and thermal stability than commonly used sulfide phosphors such as $ZnS:Cu^+$, Al^{3+} and $Y_2O_2S:Eu^{3+}$. This advantage makes these materials more chemically stable in high vacuum and under electron excitation. Therefore, there is an incessant search for new oxide phosphors with high performance for phosphor applications.[3]

Cerium oxide (CeO_2) is a well-known functional material[4] with a cubic fluorite structure, has been considered as one of the most important oxide materials because of its good thermal and chemical stability[5,6] and special optical properties[7-10] such as high refractive index, optical transparency, high dielectric constant and non-toxicity.[11] It has potential applications as an optical coating, electro-optical, microelectronic, optoelectronic devices, ion-conducting layers, electrolyte in solid oxide fuel cells,[12-14] oxygen gas sensors,[15] support in automotive catalysts,[16] ultraviolet shielding materials etc.[17] Tetravalent cerium ion (Ce^{4+}) has no 4f electrons which makes it as a promising photoluminescence (PL) host material.[18]

Recently Eu^{3+} ion doped CeO_2 phosphors have attracted much attention because of strong light absorption through the charge transfer (CT) from O^{2-} to Ce^{4+} around 370 nm.[19, 20] If the energy transfer is achieved from the CT states of CeO_2 to the doped RE ions, intense characteristic emissions are expected to be observed. The matching ionic radius of Eu^{3+} and Ce^{4+} favors the extensive solubility of europium with the ceria lattice. In this regard, a few investigations were carried out on the photoluminescence properties of Eu^{3+} doped ceria.[21-26]. Also cerium oxide (CeO_2) is well known for the large deviation in the stoichiometry due to easy reducibility of Ce^{4+} to Ce^{3+} ions. The europium substitution in cerium oxide lattice creates oxygen vacancies to compensate for the effective negative charge associated with the trivalent dopant. The luminescence in these Eu^{3+} doped ceria is mainly limited by the amount of oxygen vacancies.These oxygen vacancies act like PL quenching centers and adversely affect the PL of Eu^{3+} by seizing the radiative route of emission. In view of this, it is more difficult to achieve sizeable luminescence for any practical applications in the CeO_2 fluorite lattice. Our prime interest here is to prepare a cerium oxide based host lattice overcoming the above limitations of luminescence in the present work.

Ceria has a fluorite structure with every Ce ion surrounded by eight equatorial oxygen ions in O_h symmetry. Ideal fluorite is a simple crystal structure having a general formula AO_2. But defect fluorite structure is anion deficient with a formula, $AO_{1.75}$.[27] A fluorite (F)-type structure can accept various amounts of oxygen vacancies, from which pyrochlore (P)-type and rare earth C (C)-type structures can be derived, depending on oxygen content. The P-type structure with a general formula $A_2B_2O_7$ which belongs to the F*d*3*m* space group (Z= 8). The cubic C-type structure with a composition of A_2O_3 ($AO_{1.5}$) belongs to the space group *I*a3 (Z=16), which can also be recognized as the F-type structure with ordered oxygen vacancies in the anionic sub lattice.[28] Further, this structure may also tolerate excess anions in the presence of tetravalent lanthanides which promotes the 8-fold coordination of the Ln

sites.[29] Thus the formation of C-type phase from a defect fluorite structure incorporates more oxygen into the lattice and increases the oxygen vacancy ordering[30] on substitution of $Eu^{3+}$for Ce^{4+}. In this regard, we made an attempt to enhance the red emission of CeO_2: Eu^{3+} by choosing ceria in a C- type structure.

Though many soft chemical routes such as sol gel process,[21] hydrolysis assisted co-precipitation method,[22] chemical precipitation,[23] solid state reaction,[3, 24] solution combustion synthesis,[25,31] non hydrolytic solution route,[20] spin-on/pyrolysis technique[18] and electrochemical deposition[26] are employed in the preparation of Eu^{3+} doped ceria phosphors however they are mainly focused in the preparation of nanophosphors. As known the synthesis method and heat treatment of phosphors have a direct influence on the luminescence properties by way of changes in the crystallite size, particle size, crystallinity, surface texture and shape of particles. However, the present work is focused on the modifications of crystalline structure and cerium oxidation states on substitution of Eu^{3+} at isovalent and aliovalent sites and its influence on photoluminescence properties. The influence of this particular aspect is studied by the solid state reaction method. In this context, we have synthesized the ceria based host of the general formula, $Y_2Ce_2O_7$ and Eu^{3+} is substituted on both sites having the compositions; $Y_{1.9}Ce_2O_7$:*0.1*Eu^{3+}, $Y_2Ce_{1.9}O_7$:*0.1*Eu^{3+} via the conventional solid state reaction method to probe the influence on the structure and luminescence properties. The structure, morphology, photoluminescent properties and the electronic structure of the developed phosphors were characterized by powder X-ray diffraction, FT-Raman, transmission electron microscope, scanning electron microscope with energy dispersive spectrometer, X-ray photoelectron spectroscopy, UV-visible absorption, photoluminescence and life time measurements. It is observed that the substitution of Eu^{3+} at Ce^{4+} site induced a structural transition and decreases the Ce^{3+} oxidation states. The developed phosphors $Y_2Ce_{1.9}O_7$:*0.1*Eu^{3+} exhibit enhanced red emission of Eu^{3+} (612nm)

under the excitation of blue light 466nm than that of $Y_{1.9}Ce_2O_7$:*0.1*Eu^{3+}. In order to understand the effect of Eu^{3+} concentration onphotoluminescent properties of the as prepared $Y_2Ce_{2-x}O_7$:*x*Eu^{3+}(*x* = 0.05, 0.10, 0.15, 0.20, 0.25 and 0.50) are also studied in detail. By increasing the Eu^{3+} concentration the intra-$4f^6$ transition bands of Eu^{3+} at 466nm ($^7F_0$-$^5D_2$ transition in the blue region) is more leading than the other transition bands, which matches well with the emission of commercial GaN-LED (440-470 nm) chips. The ordering of oxygen vacancies, more distortion of Eu^{3+} at Ce^{4+} site and change of next neighbor of Eu^{3+} are some of the other factors that enhanced the luminescence. Some of these results are presented in this paper.

2. Experimental

The yttrium cerate based red phosphors: $Y_{1.9}Ce_2O_7$:*0.1*Eu^{3+}, $Y_2Ce_{1.9}O_7$:*0.1*$Eu^{3+}$and $Y_2Ce_{2-x}O_7$:*x*Eu^{3+} (*x* = 0.05, 0.10, 0.15, 0.20, 0.25 and 0.50) were synthesized by the conventional solid-state reaction technique. Y_2O_3, CeO_2, Eu_2O_3 from Sigma–Aldrich, Steinhheim, Germany with 99.99% were used as the starting materials and the precursor oxides are fine powders. These precursors were taken in the required stoichiometric ratios of Y:Ce:Eu = (1.9:2:0.1, 2:1.9:0.1 and 2:2-*x*:*x*) and mixed thoroughly in an agate mortar using acetone as the mixing medium until fine slurry was obtained.The slurry was dried by placing it in an air oven at a temperature of 100°C. The mixing and drying was repeated thrice to obtain a homogenous mixture. The homogeneous mixture was then calcined on a sintered alumina plate in an air atmosphere electrical furnace at 1400°C for 15 h. In order to ensure the completion of the reaction, the calcinations were repeated twice at 1500°C for 6 h with intermittent grinding. The temperature of the furnace is programmed with an initial heating rate of 10°C/min up to 900°C followed by a heating rate of 5°C/min to attain the desired temperatures.

The crystalline structure, the phase purity and the lattice parameter of the samples were examined by recording X-ray diffraction patterns using a PANalytical X'Pert Pro diffractometer having Ni filtered CuKα radiation with X-ray tube operating at 40 kV, 30mA and 2θ varied from 10 to 90° in 0.016° steps. The Raman spectra of the powder samples were acquired using an integrated micro-Raman system of Labram HR 800 spectrometer (Horiba Scientific) using a 633 nm helium-neon laser with a spatial resolution of 2μm to obtain the structure of the powdered samples. X-ray photoelectron spectroscopy (XPS) experiments were carried out on a KRATOS-AXIS 165 instrument equipped with dualaluminum–magnesium anodes with Mg K_α radiation (1253.6 eV) operated at 5 kV and 15 mA with a pass energy of 80 eV and an increment of 0.1 eV. The samples were degassed out for several hours in an XPS chamber to minimize air contamination to the sample surface. To overcome the charging problem, a charge neutralizer of 2 eV was applied, and the binding energy (BE) of the C1s core level (BE = 284.6 eV) of adventitious hydrocarbon was used as a standard. The XPS spectra were fitted with a nonlinear square method with the convolution of Lorentzian and Gaussian functions after a polynomial background was subtracted from the raw spectra. The selected-area electron diffraction (SAED) patterns and high-resolution electron microscopy of the samples were taken using a TECNAI $30G^2$ S-TWIN transmission electron microscope (FEI, The Netherlands) operating at 300 kV. The size and morphology of the powder particles were done by a scanning electron microscope (JEOL, JSM-5600LV) operated at 15kV. The X-ray microchemical analysis and elemental mapping of the samples were carried out using silicon drift detector–X-Max^N attached with a Carl Zeiss EVO SEM. The absorption characteristics of the synthesized samples were studied in the wavelength range 200-800nm by a Shimadzu, UV-3600 UV-Vis spectrophotometer using barium sulphate as a reference. The photoluminescence excitation and emission spectra of the prepared samples were obtained using a Spex-Fluorolog DM3000F spectrofluorimeter with a

450W xenon flash lamp as the exciting source. Luminescence life time of the phosphors was recorded by the phosphorimeter attached to Fluorolog®3 spectrofluorimeter. All the measurements were carried out at room temperature.

3. Results and discussion

3.1 Effect of Eu^{3+} doping on the A and B sites of yttrium cerate ($Y_2Ce_2O_7$) red phosphors.

A careful analysis of the XRD patterns is done in order to understand any structural and crystallite size modification on the effect of Eu^{3+} doping on the A and B sites of $Y_2Ce_2O_7$ and the corresponding diffraction patterns are shown in Fig. 1. It revealed that none of the samples was found to have pyrochlore (P) type structure though the stoichiometry of the compounds is P-type composition, as the typical super-lattice peaks at $2\theta \approx 14^\circ, 27^\circ, 36^\circ, 50^\circ$ etc corresponding to pyrochlore lattice were absent. The diffraction pattern of the Eu^{3+} doping on the B-site (Ce^{4+}) shows several extra weak diffraction peaks other than those of cubic fluorite (F) type phase on the contrary these superlattice peaks are absent on the A-site (Y^{3+}) doped and the host pattern (Inset of Fig. 1). Since the diffraction lines of the $Y_2Ce_{1.9}O_7$:*0.1*Eu^{3+}samples were successfully indexed on a basis of the rare-earth C-type phase in accordance with the powder diffraction file no 01-074-7393, $Y_2Ce_{1.9}O_7$:*0.1*Eu^{3+} can be recognized to be a nonstoichiometric C-type compound containing excess oxygen.[28] Upon Eu^{3+} doping on A and B sites of $Y_2Ce_2O_7$, there is no significant peak shift for the Y^{3+} substitution while that of the Ce^{4+} substituted one shifts to a lower angle to a large extent in reference to the host $Y_2Ce_2O_7$(Inset of Fig.1). These peak position shifts is in accordance with the differences in ionic radii of Y^{3+} (0.1019 nm), Ce^{4+} (0.097 nm) and Eu^{3+} (0.1066 nm) in 8-fold co-ordination and also further evidences the anticipated Eu^{3+} substitution on the A and B sites.The lattice constant of $Y_2Ce_{1.9}O_7$:0.1Eu^{3+} was calculated to be 10.7764 Å, while that of $Y_{1.9}Ce_2O_7$:0.1$Eu^{3+}$of the typical defect fluorite type structure was 5.3859Å. The ionic radius

of Ce^{4+} is much smaller than that of the Eu^{3+} and is close to that of the Y^{3+}, on the expected linesa larger lattice constant of $Y_2Ce_{1.9}O_7$:0.1Eu^{3+} was observed, which may also be ascribed to excess oxygen content in the C-type structure in addition to the higher cation substitution.The average crystallite size can be estimated from the Scherer formula

$$D_{hkl} = k\lambda/\beta \cos(\theta) \quad (1)$$

where λ is the X-ray wavelength (0.154056 nm), β is the full width half maximum (in radian), θ is the diffraction angle, k is a constant (0.89), and D_{hkl} represents the size along (hkl) direction.The obtained crystallite size values show a marked difference between the $Y_{1.9}Ce_2O_7$:0.1Eu^{3+} (123 nm) and $Y_2Ce_{1.9}O_7$:0.1Eu^{3+} (135 nm) which also hints out the structural transition. From the XRD analysis, it is clear that the doping of higher ionic radii of Eu^{3+} ions a tCe^{4+}site induces a structural transition from a defect fluorite to C-type structure.

Further structural investigation of the prepared samples was carried out by Raman spectroscopy. Since X-ray diffraction is more sensitive to disorder in the cation sublattice than the anion sublattice, the X-ray scattering power of oxygen is much less than the cations. But, Raman spectroscopy is very sensitive to metal-oxygen vibration modes than the metal-metal vibration modes. Hence Raman scattering is an excellent, non-destructive, and rapid analysis technique for investigating phonon structure of materials. Therefore, M. Glerup et al says that the Raman spectroscopy is an excellent tool to analyse the extent of disorder in different phases.[32] Raman spectroscopic information provides an explicit way to distinguish between a C-type material, defect fluorite material, so called pyrochlore with the radius ratio close to the pyrochlore and defect fluorite border. According to factor group analysis,[33] Raman spectra of a pyrochlore structure has six Raman active modes which are $\Gamma = A_{1g}+E_g+4F_{2g}$ and the only Raman active mode of the fluorite-type structure is F_{2g}. Fig. 2 shows Raman spectra for the $Y_2Ce_2O_7$, $Y_{1.9}Ce_2O_7$:*0.1*Eu^{3+} and $Y_2Ce_{1.9}O_7$:*0.1*Eu^{3+} samples.

From the literature study, the pure $Ce_{0.9}O_2$:*0.1*Eu^{3+} displays an intense band at 466 cm^{-1} assigned to the symmetric mode of the O atoms around each Ce^{4+} that is the single allowed Raman mode with F_{2g} symmetry in metal oxides with a fluorite structure.[34] The Raman spectra of the host $Y_2Ce_2O_7$ showed a distinct band with a wave number of 468 cm^{-1}, which was assigned to the F_{2g} mode due to the symmetrical stretching of the metal oxygen vibrational mode in 8-fold co-ordination.[35, 36] Upon Eu^{3+} doping the F_{2g} mode at 468cm^{-1} is vanishingly observed in the Y^{3+} site substituted Raman spectra and completely disappears in the Ce^{4+} site substituted one. The characteristic Raman modes of C-type structure are observed more prominently at 262, 385, 490 and 580 cm^{-1} compared to Y^{3+} site substituted samples. Similar Raman modes are observed in the literature of C-type structure compounds.[37, 38] The distinct mode around 490 cm^{-1} was assigned to the T_{2g} mode of the rare earth C-type structure. Thus the substitution of higher ionic radii like Eu^{3+} at Ce^{4+} site induces a structural transition from the defect fluorite to C-type. This result is in confirmative with the XRD analysis. The $Y_{1.9}Ce_2O_7$:*0.1*Eu^{3+} sample under study exhibits very broad humps at 262, 385, 490 and 580 cm^{-1} implying that the sample is not completely either in C-type or defect fluorite type structure. Though XRD of the $Y_{1.9}Ce_2O_7$:*0.1*Eu^{3+} indicates formation of defect fluorite type structure. However Raman analysis points out to the formation of a biphasic that of C-type and defect fluorite structure.

In order to understand the changes in the valency chemistry and binding energy of the cerium XPS analysis is carried out. The recorded XPS spectra were charge-corrected with respect to the C (1s) peak at 284.723 eV. The XPS Ce $3d_{5/2}$ and $3d_{3/2}$ doublets are commonly denoted u and v and extend in the energy range of 880-920 eV.[39-41] Fig. 3 shows the XPS spectra for Ce 3d of $Y_2Ce_2O_7$, $Y_{1.9}Ce_2O_7$:*0.1*Eu^{3+} and $Y_2Ce_{1.9}O_7$:*0.1*Eu^{3+} phosphors, the fitted curve and the corresponding deconvoluted peaks. The spectrum was deconvoluted to give the individual spin-orbit doublet of $3d_{3/2}$ and $3d_{5/2}$, and the sum of the deconvoluted peaks was

used to produce the fit of actual data. The deconvoluted Ce (3d) spectrum is relatively complex due to the presence of Ce in 3+ and 4+ oxidation states as well as multiple d-splitting. If Gaussian function is used to model the peaks, there are three parameters for each peak i.e. energy, full width half maximum (FWHM) and area. XPS results indicate that Ce is in mixed valance state of 3+ (885.50, 904.07 ± 0.7eV which is denoted as v' and u' respectively) and 4+ (882.70, 888.96, 898.20, 901.30, 907, 916.7± 0.7eV which is denoted as v, v'', v''', u, u'' and u''').[23] The v and v'' peaks are attributed to the bonding and antibonding states arising from the multielectron configuration of $3d^9 4f^2 (O\ 2p^4)$ and $3d^9 4f^1 (O\ 2p^5)$ Ce^{4+}, and the v''' peak to a $3d^9 4f^0 (O\ 2p^6)$ Ce^{4+} final state.[41-44] The v' peak corresponds to the $3d^9 4f^1$ $(O\ 2p^6)$ Ce^{3+} final state. The same explanation holds true for the series of u structures of the $3d_{3/2}$ level. However, one pair (denoted u_0 and v_0) is hardly observed because it is a shoulder on the Ce^{4+} 3d spectrum. The integrated area under the curve of each deconvoluted peak was used to calculate the concentration of Ce^{3+} ions and is given as[23, 41]

$$[Ce^{3+}] = \frac{A_{v'} + A_{u'}}{\sum A_i} \qquad (2)$$

where $\sum A_i$ is the total integrated area.

H. Baocited that the major difference of the Ce 3d XPS features between Ce(IV) oxide and Ce(III) oxide is that Ce 3d XPS spectrum from Ce(IV) oxide consists of three pairs of spin-orbit doublets whereas that from Ce(III) oxide only two pairs of spin-orbit doublets.[45] The Ce XPS spectrum shows clear three-pairs of spin-orbit doublets which implies that Ce(IV) dominates in our systems. At the same time it was found that the concentration of Ce^{3+} is found to be more in $Y_{1.9}Ce_2O_7$:*0.1*Eu^{3+} (17.1%) than in the host $Y_2Ce_2O_7$ (14.1%) and $Y_2Ce_{1.9}O_7$:*0.1*Eu^{3+} (13.1%). The variation of Ce^{3+} states is also well observed in the absorbance spectra and its influence on the luminescence properties are discussed in the later part of the text.

Fig. 4 shows the scanning electron micrographs of as prepared samples which are synthesized using the solid state reaction route. The microstructure shows increasing trend of particle size for the Ce^{4+} substituted one than that of the Y^{3+} and the host. The increase in crystallite size on structural transition from defect fluorite to C-type structure as observed in the XRD analysis is evidently reflected in the microstructure. The particles are slightly agglomerated with an average size of 1–3 μm.

The UV-vis absorption spectra of $Y_2Ce_2O_7$, $Y_{1.9}Ce_2O_7$:*0.1*Eu^{3+} and $Y_2Ce_{1.9}O_7$:*0.1*Eu^{3+} are presented in Fig. 5. There is a strong absorption band below 400 nm in the spectra with maxima at 242, 302 and 340 nm which are mainly attributed to the charge-transfer transition from O^{2-}-Ce^{3+}, O^{2-}-Ce^{4+} and inter band transfer respectively[46] in the samples. In addition the absorbance due to charge transitions from O^{2-}-Ce^{3+} for $Y_{1.9}Ce_2O_7$:*0.1*Eu^{3+} is relatively more than the host and the Ce^{4+} substituted one. This observation also points out the variation in the Ce^{3+} states with the change of Eu^{3+} site substitution. The absorption spectra of $Y_{1.9}Ce_2O_7$:*0.1*Eu^{3+} phosphors exhibited a red shift compared with that of the host $Y_2Ce_2O_7$ while $Y_2Ce_{1.9}O_7$:*0.1*Eu^{3+} exhibited a blue shift. This shift in the absorption band can be explained as that there always coexisted some amount of Ce^{3+} and the valance change might have some additional contribution to the absorption spectra.[23, 47] When Eu^{3+} was doped into the B (Ce)-site of $Y_2Ce_2O_7$, the Ce^{3+} ions may be replaced by Eu^{3+}ions, and also the change from Ce^{4+} to Ce^{3+} ions will decrease due to the structural transition from defect fluorite to C-type structure. Hence the blue shifting arises. While Eu^{3+} was doped into the A (Y)-site of $Y_2Ce_2O_7$, the Ce^{3+} ions in the lattice somehow maintained and induce the increase of Ce^{3+} ions in the lattice due to defect formation in the oxygen deficient fluorite structure, which increases the change from Ce^{4+} to Ce^{3+} ions and hence exhibited the red shift in the absorption spectrum. This Ce^{3+} oxidation state assessment from the absorption spectra is in good agreement with the XPS results.

The luminescent properties were investigated by recording the PL spectra of $Ce_{0.9}O_2$:*0.1*Eu^{3+}, $Y_{1.9}Ce_2O_7$:*0.1*Eu^{3+} and $Y_2Ce_{1.9}O_7$:*0.1*Eu^{3+} phosphors at room temperature under the identical instrumental conditions. The excitation spectra were measured by monitoring the peak intensity at 612 nm. The excitation spectra of the above samples, as shown in Fig. 6 include a weak broad band region from 280 to 389 nm and some sharp peaks at 380, 394, 414 and 466 nm which are assigned to the intra-$4f^6$ transition absorptions of Eu^{3+} in the host lattice: $^7F_0$ to $^5G_{2\text{-}4}$ and $^5L_7$, $^5L_6$, $^5D_3$ and $^5D_2$ respectively.[48-51] Since the O^{2-} - Eu^{3+} charge transfer (CT) states lie in much shorter wavelength region around 250-300 nm as reported[52, 53] and CeO_2 has a band gap around 3.4 eV (~370 nm),[54] the broad band in the UV region of the excitation spectra should be attributed to the charge transfer transition of Ce^{4+} - O^{2-} group. From the excitation spectra, it was found that for $Y_2Ce_{1.9}O_7$:*0.1*Eu^{3+} samples, the intra-$4f^6$ transition of Eu^{3+}, especially the one at 466 nm are more dominant than the $Ce_{0.9}O_2$:*0.1*Eu^{3+} and $Y_{1.9}Ce_2O_7$:*0.1*Eu^{3+} samples.

The PL emission spectra for the as prepared samples excited at 466 nm are shown in Fig. 7. The spectra consist of a series of well resolved peaks at 580, 593, 612, 630, 654, 682, 696 and 711 nm, which can be assigned to $^5D_0$-^7F_J (J=0, 1, 2, 3 and 4) transitions of Eu^{3+} ions, namely, the $^5D_0$-$^7F_0$ (580 nm), $^5D_0$-$^7F_1$ (593 nm), $^5D_0$-$^7F_2$ (612 and 630 nm), $^5D_0$-$^7F_3$ (654 nm) and $^5D_0$-$^7F_4$ (682, 696 and 711 nm), respectively.[55] As per J-O theory,[56, 57] the emission lines are a cumulative effect of magnetic dipole (MD) transition and electric dipole (ED) transition, depending on the specific environment of Eu^{3+} in any matrix. According to the J-O theory, ED transition ($^5D_0$-$^7F_2$) centred at about 612 and 630 nm, is only allowed in the absence of inversion symmetry and is hypersensitive to the local electric field whereas the MD transition ($^5D_0$-$^7F_1$) with emission at 591 nm is a magnetic dipole allowed transition, which is insensitive to the crystal environment.In the present study the electric dipole transition intensity at 612 nm was found to be higher which indicates that Eu^{3+} mainly occupies the

lattice sites that reduce the O_h symmetry of the C-type structure. The emission intensities of $Y_2Ce_{1.9}O_7$:*0.1*Eu^{3+} sample becomes 3.8 times greater than the $Ce_{0.9}O_2$:0.1Eu^{3+} and $Y_{1.9}Ce_2O_7$:*0.1*Eu^{3+}. From decay curves shown in the Fig. 8, the life time values of $^5D_0$-$^7F_2$ transitions for $Y_2Ce_{1.9}O_7$:*0.1*Eu^{3+} and $Y_{1.9}Ce_2O_7$:0.1Eu^{3+} are 0.640 and 0.598 ms respectively.

The enhancement of photoluminescence properties of the present phosphors can be explained like this. Luminescence properties are mainly influenced by the crystallographic structures, symmetry of the activator and its surroundings, ordering of the activator in the lattice, etc. As known a trivalent substitution like Eu^{3+} in a simple fluorite lattice CeO_2 leads to the formation of oxygen vacancies for charge compensation. These oxygen vacancies act like PL quenching centres and reduce the radiative transitions which limit the sizeable enhancement of luminescence in the simple fluorite lattice. In the present case the Eu^{3+} substitution at A and B sites demonstrates greatly the influence of the structure and the symmetry of Eu^{3+} on the luminescence properties of the phosphor materials. Though the Eu^{3+} substitution at A-site would not create any oxygen vacancies but holds the biphasic nature of defect fluorite and C-type structure which inherits the disordered oxygen vacancies and which adversely affect the luminescence. Further the oxygen vacancies favour the reduction of Ce^{4+} to $Ce^{3+}$and by which Ce^{3+} states are more observed in the A-site substitution. In such a situation the probability of Eu^{3+} can exist more as Ce^{3+}-O^{2-}-Eu^{3+}. The ionic size of the Eu^{3+} is close to the Ce^{3+} rather than the size of Ce^{4+}. It is expected that the Ce^{3+}-O^{2-}-Eu^{3+} has more symmetry situation than that of the Ce^{4+}-O^{2-}-Eu^{3+} configuration. Under similar condition the increased symmetry of Eu^{3+} favours the magnetic dipole (MD) induced emission. This is further evidenced by the asymmetric ratio $I(^5D_0$-$^7F_2)/I(^5D_0$-$^7F_1)$ which provides the information on the site symmetry of Eu^{3+}. This value (3.5) is also observed to be lower than the (3.9) B-site substituted phosphor. In a nutshell disorder in the lattice, oxygen vacancies and increase in Ce^{3+} oxidation states adversely affected the luminescence in A-site

substitution. On the contrary the Eu^{3+} on the B-site substitution made a structural variation from defect fluorite to C-type structure. Literature indicates that heavily doped higher ionic radii rare-earths strongly influence the transformation from fluorite to C-type structure and the oxygen vacancy ordering in the lattice.[58] The higher degree of ordering with substitution blocks the oxygen vacancies and mobility in the lattice. In turn this phenomenon inhibits the reduction of Ce^{4+} to Ce^{3+}. The XPS result supports the decreased amount of Ce^{3+} states in the B-site substitution. Under this situation the probability of existence of Eu^{3+} increases in Ce^{4+}-O^{2-}-Eu^{3+} configuration reducing the Eu^{3+} symmetry as pointed out above. C-type structure is formed out of 8 unit cells of the fluorite structure by removing 25% of oxygen ions with introducing small ionic shifts. It is also reported that the C-type structures derived from the fluorite structure of Y^{3+} doped CeO_2 tolerates excess oxygen having a larger oxygen co-ordination of Ce^{4+}.[37] Further the presence of oxygen vacancy induces the distortion of the Ce polyhedra by way of oxygen relaxation towards the vacancies. The above observations indicate that the Eu^{3+} in the transformed C-type lattice experiences more distortion and ordering in the lattice. The obtained relatively higher asymmetric ratio value further confirms the above assessment in comparison with the A-site substitution. The $^5D_0$ life time of Eu^{3+} for the Ce^{4+} substitution is higher than the Y^{3+} substituted one, indicating more uniform distribution of Eu^{3+} due to structural ordering in the lattice. All these factors enhanced the PL properties significantly for the B-site substituted compound; hence further investigations are confined to the $Y_2Ce_{2-x}O_7$:$x$$Eu^{3+}$ with respect to the variation of Eu^{3+} concentration.

3.2 Photoluminescent studies of $Y_2Ce_{2-x}O_7$:xEu^{3+}(x = 0.05, 0.10, 0.15, 0.20, 0.25, 0.50) Red phosphors

The powder XRD patterns of $Y_2Ce_{2-x}O_7$:$x$$Eu^{3+}$($x$ = 0.05, 0.10, 0.15, 0.20, 0.25, 0.50) phosphors are given in Fig. S1. The XRD patterns of the Eu^{3+} doped samples can be indexed completely to the C-type structure as discussed in the previous section. No impurity peaks

were observed in the XRD patterns upon different doping of Eu^{3+} which suggests doping of a small percentage of Eu^{3+} ions does not change the crystal structure. The cell parameters, in conformity with the C-type phase are given in Table 1.

It can be seen from the cell parameters that the lattice parameter increases with the increase of Eu^{3+} concentration as expected, since the ionic radius of Eu^{3+} (r = 0.1066 nm, when coordination number (CN) = 8) is larger than that of the Ce^{4+} (r = 0.097nm, when CN = 8). This further confirms that the substitution of Eu^{3+} takes place in the lattice site of Ce^{4+}. The average crystallite size of the as prepared samples is found to be nearly constant around 135nm which also implies there is no structural variation with Eu^{3+} substitution.

Fig. 9 shows the Raman spectra for the $Y_2Ce_{2-x}O_7$:$x$$Eu^{3+}$($x$ = 0.05, 0.10, 0.15, 0.20, 0.25, 0.50) phosphors. As discussed in the first section, it is clear that the Raman spectrum for the B (Ce^{4+}) site substituted samples exhibits the characteristic modes of C-type structure.The modes gradually become broader with decreased intensity upon Eu^{3+} substitution. As a consequence to that, the FWHM of the modes increases indicating the increasing oxygen vacancy formation. Typically the FWHM values for 385 cm-1 mode is listed in Table1.

Fig. S2 presents the XPS spectra of Ce 3d core levels for $Y_2Ce_{1.5}O_7$:*0.5*Eu^{3+} phosphors. Six peaks of the spectrum refer to three pairs of spin-orbit doublets, which can be identified as characteristic of Ce^{4+} 3d final states. In addition the characteristics peaks corresponding to the Ce^{3+} species are also observed. By fitting the curves and then calculating the area of the fitted peaks, we conclude that the concentration of Ce^{3+} in $Y_2Ce_{1.5}O_7$:*0.5*Eu^{3+} phosphor decreased compared to the lower substituted one (x = 0.10) and is found to be 11.5%. This decrease of Ce^{3+} states can be attributed to the increased ordering of the oxygen vacancies in the lattice inhibiting the cerium reduction.

Electron diffraction patterns from a single particle of $Y_2Ce_{1.8}O_7$:*0.2*Eu^{3+} and $Y_2Ce_{1.5}O_7$:*0.5*Eu^{3+} red phosphors are shown in Fig. S3. The SAED pattern shows a poly crystalline structure and is consistent with C-type unit cell indicating diffraction maxima with many weak diffraction spots of the superlattice planes. The chemical composition of the phosphors was checked by energy dispersive spectrophotometer (EDS) analysis attached with TEM and identifies the presence of all the expected elements which is shown in Fig. S4. This further confirms the homogeneity of the phase formed. The compositions derived from the micro-chemical analysis of the phosphors are in close agreement with the stoichiometry of the formulae.

Fig. S5 shows the typical SEM microstructure of $Y_2Ce_{2-x}O_7$:$x$$Eu^{3+}$ (x = 0.05, 0.10, 0.15, 0.20, 0.25, 0.50) red phosphors. The micrographs show slightly agglomerated particles in the range 1-3µm. Elemental mapping analysis of typical $Y_2Ce_{1.5}O_7$:*0.50*Eu^{3+}red phosphor calcined at 1500˚C for 12 hrs is shown in Fig.10. This confirms that all the elements are uniformly distributed in the lattice.

The UV-vis absorption spectra of the $Y_2Ce_{2-x}O_7$:$x$$Eu^{3+}$ (x = 0.05, 0.10, 0.15, 0.20, 0.25, 0.50) is presented in Fig. 11. The absorption spectra of all the samples exhibit a strong absorption band below 400nm in the UV region which is mainly attributed to the charge-transfer transition from O^{2-} (2p) to Ce^{4+} (4f) orbital's[23] in $Y_2Ce_{2-x}O_7$:$x$$Eu^{3+}$.The absorption spectrum exhibited a blue shift compared with that of the lower concentration of Eu^{3+}. Blue shift is seen with increasing Eu^{3+} concentration and the band gap were calculated from the absorption spectra using Shapiro's method by extrapolating the onset of absorption to the wavelength axis and is given in the Table 2. The literature survey reveals that the blue shift in the bandgap can occur due to several factors such as the grain size effect,[59] stress in the matrix,[60] amorphous nature of the material[61] and oxygen vacancies on the outermost surface.[18,35,42-43] In our case, however, significant blue shift was observed and there was no

detectable grain size reduction. Hence grain size effect had not played an important role in the observed blue shift. The diffraction pattern of the samples shows highly crystalline; hence it is not due to amorphous nature. Hence the blue shift in the UV-vis absorption spectra may be attributed to the decrease of valence change from Ce^{4+} to Ce^{3+}as indicated by the XPS results and the increasing oxygen vacancies in the lattice.

Fig. 12 and Fig. 13 show the excitation and emission spectra of $Y_2Ce_{2-x}O_7$:xEu^{3+} (x = 0.05, 0.15, 0.20, 0.25, 0.50) phosphors. One of the remarkable changes in the excitation spectra is the enhanced f-f transition intensity prominently at 466 nm. The emission spectra shows gradual increase in red emission intensities (612 nm) and it increased with increase in Eu^{3+} doping concentration. Eventually the intensity of 50 mol% of Eu^{3+} becomes 8.5 times greater than the lower one i.e no concentration quenching is observed. The intensity (R/O) ratio (which is also known as asymmetry ratio) is a measure of the degree of distortion from the inversion symmetry of the local environment of the Eu^{3+} ion in the lattice. The R/O value can be calculated using the following equation

$$Asymmetric\ ratio = \frac{\mathrm{I(5D0 \rightarrow 7F2)}}{\mathrm{I(5D0 \rightarrow 7F1)}} \quad (3)$$

and the values of the as prepared samples are tabulated in Table. 2

It can be clearly observed that the intensity ratio increases from 3.93 to 4.42 with the increase of the Eu^{3+} concentration under the excitation of 466nm. The results imply that the prologue of Eu^{3+} into the $Y_2Ce_{2-x}O_7$ would perturb the host structure i.e most of the Eu^{3+} ions would occupy sites without inversion symmetry. It may be also due to the oxygen deficiencies in the Eu^{3+} doped yttrium cerate particles. This is because Ce can exist in 3+ and 4+ oxidation states and also the presence of Y^{3+} ions, the coexistence of (Ce^{3+}-O-Eu^{3+}), (Ce^{4+}-O-Eu^{3+}) and (Y^{3+}-O-Eu^{3+}) arrangements in the crystalline environment is possible. The size of the Eu^{3+} ion (0.095 nm) is close to that of Ce^{3+} (0.1.02 nm) rather than to the size of Ce^{4+} (0.087 nm),

which implies that the (Ce^{3+}-O- Eu^{3+}) configuration has more symmetry as compared with the (Ce^{4+}-O-Eu^{3+}) configuration. The R/O intensity ratio suggest that the higher mol% of Eu^{3+} ions are at Ce^{4+} sites and generates lattice distortion of the local environment around Eu^{3+} ions and thus favours the electric dipole induced emission ($^5D_0$-$^7F_2$). On increasing the Eu^{3+} concentration, the Ce^{3+} concentration decreases, at the same time Ce^{4+} concentration is more predominant, as also supported from the XPS results, and thus the asymmetric (Ce^{4+}-O-Eu^{3+}) configuration probability in the lattice increases, which suggests that ED transition is more favourable than MD transition.

C-type structures derived from defect fluorite lead to the formation of two different sets of shorter and longer cation-cation distances whereas the only one cation-cation distance is observed in fluorite structures.[58] The different distances in C-type are caused by the occupation of the oxygen in between the two cations. The transformation drives the oxygen vacancy ordering in which the smaller cations are in octahedral co-ordination and the second one is either in 8-fold coordinated as in the fluorite structure or 7-hold or both. In the present study the results of XRD and Raman studies indicate the formation of C-type structure with exccess oxygen. In such a situation Y^{3+} ion is in octahedral coordination whereas Ce^{4+} is in 8-fold or lesser co-ordination. Further our results confirm the substitution of Eu^{3+} at the Ce^{4+} site. The Eu^{3+} can exists mainly in the configuration Y^{3+}-O^{2-}-Eu^{3+}-O^{2-}-Y^{3+}-O^{2-}-Ce^{4+} repetitively due to cation ordering linked to the oxygen vacancy ordering. This facilitates the more uniform distribution of Eu^{3+} in the lattice. The emission intensities increase with increase of Eu^{3+} concentration up to 50 mol.% without quenching. As known concentration quenching takes place mainly through cross relaxation mechanism among Eu^{3+} ions when the distance between them reduces to a critical level. When the Eu^{3+}- Eu^{3+} distance falls below this critical level, the excited energy of the activator is lost by non-radiative energy transfer by the creation of some oxygen vacancy defects in the host or Eu^{3+}-Eu^{3+} interaction. In

addition the multiphonon assisted non-radiative energy transfer should also contribute for the quenching.[49, 62] Generally the concentration quenching is observed mainly due to the reduction below the critical level distance in most of the host lattices. However in the present system, there is a preferential cation ordering linked to the oxygen vacancy ordering which facilitates the uniform distribution of Eu^{3+} ions in the lattice leading to preventing the formation of clustering of ions. Thus the cross relaxation between Eu^{3+}-Eu^{3+} ions is reduced and allowing substitution of higher concentration of Eu^{3+} in this type of lattice. Therefore no concentration quenching is observed upto 50 mol % of Eu^{3+}. Whereas concentration quenching is observed in fluorite lattice CeO_2 beyond 15 mol% of Eu^{3+} doping.[23] Such preferential Eu^{3+} occupancy is absent in the disorder lattice of CeO_2 by which Eu^{3+}-Eu^{3+} distance decreases on higher substitutions leading to an effective energy transfer between the neighbouring ions. Hence the excited state moves to the quenching sites dissipating the energy non-radiatively. As a result concentration quenching takes place in in CeO_2 lattice beyond 15 mol% of Eu^{3+} doping.

In order to assess the site symmetry and luminescence behavior of Eu^{3+} ions in $Y_2Ce_{2-x}O_7$ (x = 0.05, 0.20, 0.25 and 0.50) was carried out for typical compositions by calculating the Judd-Ofelt intensity parameters Ω_t (2, 4 & 6). These intensity parameters provide the radiative probabilities of the activator ions in different hosts. Ω_2 signifies the polarization and asymmetric behavior of the activator and the ligand whereas the other two parameters depend on the long range effects. These parameters $\Omega_{2\text{-}4}$, branching ratio (β) and stimulated emission cross section (σ) were determined as described elsewhere[31, 62] and the calculation procedure was given in the supplementary information (SI). The obtained intensity parameters were listed in Table 3. The Ω_2 value is most sensitive to the asymmetric environment of the Eu^{3+} site. The value of Ω_2 increases with Eu^{3+} concentration indicates increasing asymmetric nature of Eu^{3+} in this host which is also evidenced by the higher asymmetric ratio (Table 2).

It is to be noted here that the order of the Ω_t parameters in general is $\Omega_2 < \Omega_4$ but in the present system the trend for the Ω_t parameters is $\Omega_2 > \Omega_4$. This change in trend of the intensity parameters in this system is in agreement with those reported by Kumar et. al. This implies that the efficiency for the $^5D_0$-$^7F_2$ transition becomes weak at the cost of the $^5D_0$-$^7F_1$ transition.[31] The emission intensity could also be characterized by the Ω_4 parameters. The continuous increase of Ω_4 parameter with Eu^{3+} concentration infers the efficiency for the $^5D_0$-$^7F_2$ transitions. This is further supported by the dominant value of the branching ratio (β) for the $^5D_0$-$^7F_2$ transition than the other transitions. The emission cross section values (σ) changes contrastingly for $^5D_0$-$^7F_1$ and $^5D_0$-$^7F_2$ transitions. The assessment of J-O intensity parameters indicates the ionic nature of Eu^{3+} ion at more asymmetric site in the lattice.

Fig. 14 presents the decay curves for $^5D_0$-$^7F_2$ (λ_{em}:612 nm) transition of $Y_2Ce_{2-x}O_7$:xEu^{3+} (x = 0.05, 0.20, 0.25, 0.50) phosphors under an excitation of 466 nm. All the decaycurves can be fitted well with a single exponential function:$I = A_1\exp(-x/\tau)$ where I, τ and A are intensity, decay time and fitting parameter, respectively. Here it is observed that the luminescence decay time of red emission (612 nm) of $Y_2Ce_{2-x}O_7$:xEu^{3+} (x = 0.05, 0.20, 0.25, 0.50) phosphors are listed in Table 3. The lifetime of $^5D_0$ excited state is mainly contributed by the radiative and non-radiative decay rates. As the Eu^{3+} content increases, the mean life time prolongs tediously under the excitation due to the partition of more Eu^{3+} ions in the yttrium cerate lattice due to cation ordering as discussed above. The quantum efficiency were calculated from the life time values (SI) and is found to be in the range 10-14 % with increase of Eu^{3+} concentration (Table 3). These values are slightly better than the well-known europium doped $CaMoO_4$.[63]

With the purpose of red phosphor application for white light LEDs with blue GaN-based chips as excitation source, the emission spectra of $Y_2Ce_{1.5}O_7$:*0.50*Eu^{3+} and the commercial red phosphor (Y_2O_3:Eu^{3+}) from Philips under the same excitation of 466 nm

radiation (blue region) are compared as shown in Fig.15. It is observed that the red emission intensity of $Y_2Ce_{1.5}O_7$:*0.50*Eu^{3+} is slightly greater than that of commercial red phosphor. This clearly demonstrates that the present $Y_2Ce_{1.5}O_7$:*0.50*Eu^{3+} is a promising red phosphor under blue light excitation for the phosphor converted white LEDs.

4. Conclusions

A new series of red phosphor materials: $Y_{1.9}Ce_2O_7$:*0.1*Eu^{3+}, $Y_2Ce_{1.9}O_7$:*0.1*Eu^{3+} and $Y_2Ce_{2-x}O_7$:*x*Eu^{3+} (x = 0.05, 0.10, 0.15, 0.20, 0.25, 0.50) were prepared by the conventional solid state route. The Eu^{3+} substitution at Ce^{4+} site induced a structural transition from a defect fluorite to C-type structure whereas substitution at Y^{3+} site have biphasic nature of defect fluorite and C-type. The structural transition enhanced the Eu^{3+} luminescence on account of increased oxygen vacancy ordering, reduction in Ce^{3+} oxidation states and distortion of the environment. Further the structural transition allowed increased Eu^{3+} doping concentration without quenching (up to 50 mol.%) and its life time which are mainly attributed to the uniform distribution of Eu^{3+} ions in the lattice due to cation ordering linked with oxygen vacancy. The present study suggests that sizeable Eu^{3+} luminescence in cerium based lattice can be achieved under blue light excitation which matches well with the emission of commercial GaN-LED (440-470 nm) chips. Thus these phosphors make them suitable as a promising red phosphor under blue light excitation for WLED applications.

Acknowledgments

The authors would like to acknowledge International Centre for Diffraction Data (ICDD), USA, the Councilof Scientific and Industrial Research (CSIR Net Work Project SURE CSC0132), New Delhi, Government of India, for the research facilities and financial support. We would like to acknowledge the support of Jiji. S. G from the Department of

Optoelectronics, University of Kerala for the Raman analysis and B. M. Reddy from IICT, Hyderabad for the XPS analysis.

References

1. B. Alexander, M.G.Leonid, V. S. Oksana, S. Joachim, *Adv. Funct. Mater.* 2009, **19**, 1819.

2. S. Som, S. Dutta, Vijay Kumar, Vinod Kumar, H. C. Swart, S. K. Sharma, *J. Lumin.* 2014, **146**, 162.

3. X. Liu, S. Chen, X. Wang, *J. Lumin.* 2007, **127**, 650.

4. H. Guoa, Q. Yanmin, *Applied Surface Science.* 2008, **254**, 1961.

5. X. D. Wu, C. R. Dye, R. E. Muenchausen, S. R.Foltyn, M.Maley, A. D.Rollett, A. R. Garcia, N. S. Nogar, *Appl. Phys. Lett.* 1991**, 58**, 2165.

6. H. Y. Lee, S. Kim, Y. P. Hong, Y. C. Lee, Y. H. Park, K. H. Ko, *Surface and Coatings Technology.* 2003, **173**, 224.

7. D. Barreca, G. Bruno, A. Gasparotto, M. Losurdo, E. Tondello, *Materials Science and Engineering: C.* 2003**, 23**, 1013.

8. A. K. Bhosale, P. S. Shinde, N. L. Tarwal, R. C. Pawar, P. M. Kadam, P. S. Patil, *Electrochimica Acta.* 2010, **55**, 1900.

9. S.Gnanam, V. Rajendran, *Journal of Nanoparticles*. 2013**,** Article ID 839391, 6 pages

10. P. Patsalas, S. Logothetidis,C. Metaxa, *Appl. Phys. Lett.* 2002, **81**, 466.

11. R. P. Netterfield, W. G. Sainty, P. J. Martin, S. H Sie, *.Applied Optics.* 1985, **24**, 2267.

12. F. Zhang, S. W. Chan, J. E. Spanier, E. Apak, Q. Jin, *Appl. Phys. Lett.* 2002, **80**, 127.

13. M. Nakayama, M. Martin, *Phys. Chem. Chem. Phys.* 2009, **11**, 3241.

14. W. F. Lim, K. Y. Cheong, *Phys. Chem. Chem. Phys.* 2014, **16**, 7015.

15. Z. Zhan, S. A. Barnett, *Science.* 2005, **308**, 844.

16. H. Imagawa, A. Suda, K. Yamamura, S. Sun, *J. Phys. Chem. C.* 2011, **115**, 1740.

17. P. O. Maksimchuk, A. A. Masalov, Y. V. Malyukin, *J. Nano- Electron. Phys*. 2013, **5**, 01004.

18. S. Fujihara, M. Oikawa, *J. Appl. Phys*, 2004, **95**, 8002.

19. C. Tiseanu, B.Cojocaru, D. Avaram, V. I Parvulescu, A. V Vela-Gonzalez, Sanchez-M. Dominguez, *J. Phys. D: Appl. Phys*. 2013, **46**, 275302.

20. Z. Wang, Z. Quan, J. Lin, *Inorg. Chem.* 2007, **46**, 5237.

21. Y. Yu, D. Chen, P. Huang, H. Lin, A. Yang,Y. Wang, *J. Alloys Compd*. 2012, **513**, 626.

22. R. Srinivasan, A. Chandra Bose, *Funct. Mater. Lett.* 2011, **4**, 13.

23. A. Kumar, A. S. Karakoti, A. Schuile, S. Seal, *Langmuir.* 2009, **25**, 10998.

24. S. Kunimi, S. Fujihara, *ECS J. Solid State Sci. Tech.* 2012, **1**, R32.

25. S. Shi, M. Hossu, R. Hall, W. Chen, *J. Mater. Chem.* 2012, **22**, 23461.

26. Z. L. Wang, G. R. Li, Y. N. Ou, Z. P. Feng, D. L. Qu, Y. X. Tong, *J. Phy. Cem. C*.2011, **115**, 351.

27. A. N. Radhakrishnan, P. P. Rao, K. S. Sibi, M. Deepa, P. Koshy, *J. Solid State Chem.* 2009, **182**, 2312.

28. H. Nishino, H. Yamamura, T. Arai, K. Kakinuma, K. Nomura, *J. Ceram. Soc. Japan.* 2004, **112**, 541.

29. H. J. Rossell, H. G. Scott, *J. De Physique.* 1977, **38**, C7.

30. T. Hagiwara, Z. Kyo, A. Manabe, H. Yamamura, K. Nomura, *J. Ceram. Soc. Japan.* 2009, **117**, 1306.

31. Vinod Kumar, Vijay Kumar, S. Som, M. M. Duvenhage, O. M. Ntwaeaborwa, H. C. Swart, *Appl. Surf. Sci*. 2014, **308**, 419.

32. M. Glerup, O. F. Nielsen, F. W. Poulsen, *J. Solid State Chem.* 2001, **160**, 25.

33. V. G. Keramidas, W. B. White, *J Chem. Phys.*1973, **59**, 1561.

34. D. Devaiah, L. H. Reddy, K. Kuntaiah, B. M. Reddy, *Indian J Chem.* 2012, **51**, 186.

35. A. Nakajima, A. Yoshihara, M. Ishigame, *Phys. Rev. B.* 1994, **50**, 13297.

36. I. Kosacki, V. Petrovsky, H. U. Anderson, *J. Am. Ceram. Soc.* 2002, **85**, 2646.

37. Y. Ikuma, S. Nagasawa, N. Hayasshi, M. Kamiya, *J. Jpn. Soc. Powder Powder Metallurgy.* 2005, **52**, 599.

38. B. P. Mandal, V. Grover, M. Roy, A. K. Tyagi, *J. Am. Ceram. Soc.*2007, **90**, 2961.

39. M. P. Francis, V. R.Mastelaro, *J Phys. Chem. B*.2001, **105**, 10515.

40. E. Beche, P. Charvin, D. Perarnau, S. Abanades, G. Flamant, *Sur. Interface Anal.* 2008, **40**, 264.

41. F. L. Normand, L. Hilaire, K. Kili, G. Krill,G. Maire, *J. Phys. Chem.*1988, **92**, 2561.

42. P. O. Larsson, A. Andersson, *J. Catal.*1988, **179**, 72.

43. J. Z. Shyu, W. H.Weber, H. S. Gandhi, *J. Phys. Chem.*1988, **92** 4964.

44. C. Ho, J. C.Yu,T. Kwong, A. C.Mark,S. Lai,*Chem. Mater.*2005, **17**, 4514.

45. H. Bao, X. Chen, J. Fang, Z.Jiang, W. Huang,*Catal. Lett.*2008, **125**,160.

46. B. M. Reddy, L.Katta, G. Thrimurthulu, *Chem. Mater.*2010, **22**, 467.

47. Chen, M.-Y.; Zu, X.-T.; Xiang, X.; Zhang, H.-L.*Physica B*.**2007**, 389, 263–68.

48. M. Thomas, P. P. Rao, M. Deepa, M. R. Chandran, P. Koshy, *J. Solid State Chem.* 2009, **182**, 203.

49. S. Som, A. K. Kunti, Vinod Kumar, Vijay Kumar, S. Dutta, M. Chowdhury, S. K. Sharma, J. J. Terblans, H. C. Swart, *J. Appl. Phys.* 2014, **115,** 193101.

50. J. Wang, Y. Cheng, Y. Huang, P. Cai, S. Kim, H. J. Seo, *J. Mater. Chem. C.* 2014, **2,** 5559.

51. P. Dai, X. Zhang, M. Zhou, X. Li, J. Yang, P. Sun, C. Xu, Y. Liu, *J. Am. Ceram. Soc.* 2012, **95**, 658.

52. M. Yu, J. Lin, Y. H. Zhou, S. B. Wang, *Mater. Lett.* 2002, **56**, 1007.

53. G. Blasse, *J. Chem. Phys.* 1966, **45**, 2350.

54. A. V. Emeline, G. N. Kuzmin, D. Purevdorj, V. K. Ryabchuk, N. Serpone, *J Phys. Chem. B.* 2000, **104**, 2989.

55. M. Thomas, P. P. Rao, S. K. Mahesh, V. R. Reshmi, T. Linda Francis, P. Koshy, *J. Am. Ceram. Soc.* 2012, **95**, 2260.

56. B. R. Judd, *Phys. Rev.* 1962, **127**, 750.

57. G. S. Ofelt, *J. Chem. Phys.* 1962, **37**, 511.

58. M. Coduri, M. Scavini, M. Allieta, M. Brunelli, C. Ferrero, *Chem. Mater.* 2013, **25**, 4278.

59. Y. F. Kuo, T. Y. Tseng, *Mater. Chem. Phys.* 1999, **61**, 244.

60. R. Thomas, D. C. Due, M. N. Kamalasanan, S. Chandra, *Thin Solid Films*, 1999, **346**, 212.

61. R. Thomas, D. C. Dube, *Jpn. J. Appl. Phys.* 2000, **39**, 1771.

62. S. Som, P. Mitra, K. Vijay, K. Vinod, J. J. Terblas, H. C. Swart, S. K. Sharma, *Dalton Trans.* 2014, **43**, 9860.

63. F. Lei, B. Yan, *J. Solid State Chem*. 2008, **181**, 855.

Figure Captions

Fig. 1. Powder XRD patterns of $Y_2Ce_2O_7$, $Y_{1.9}Ce_2O_7$:*0.1*Eu^{3+} and $Y_2Ce_{1.9}O_7$:*0.1*Eu^{3+} phosphors. For $Y_2Ce_{1.9}O_7$:*0.1*Eu^{3+} additional cubic C-type peaks (denoted by #) appear in the XRD pattern (inset). The inset Fig. shows the expanded view of the peak around 2θ 28-29°.

Fig. 2. Raman spectra of $Y_2Ce_2O_7$, $Y_{1.9}Ce_2O_7$:*0.1*Eu^{3+} and $Y_2Ce_{1.9}O_7$:*0.1*Eu^{3+}phosphors.

Fig. 3. XPS spectrum of Ce(3d) for the $Y_2Ce_2O_7$,$Y_{1.9}Ce_2O_7$:*0.1*Eu^{3+} and $Y_2Ce_{1.9}O_7$:*0.1*Eu^{3+} phosphors was deconvoluted to give the individual spin-orbit doublet of $3d_{3/2}$ and $3d_{5/2}$, and the sum of the deconvoluted peaks was used to produce the fit to the actual data.

Fig. 4. Typical SEM photographs of a) $Y_2Ce_2O_7$, b) $Y_{1.9}Ce_2O_7$:*0.1*Eu^{3+} and c) $Y_2Ce_{1.9}O_7$:*0.1*Eu^{3+} phosphors. The particles are slightly agglomerated and there is a broad distribution of particle size with an average size of 1-3 μm.

Fig. 5. UV-vis absorption spectra of $Y_2Ce_2O_7$, $Y_{1.9}Ce_2O_7$:*0.1*Eu^{3+} and $Y_2Ce_{1.9}O_7$:*0.1*Eu^{3+} phosphors. The absorption spectra of $Y_{1.9}Ce_2O_7$:*0.1*Eu^{3+} phosphor exhibited a red shift compared with that of the host $Y_2Ce_2O_7$ while $Y_2Ce_{1.9}O_7$:*0.1*Eu^{3+} phosphors exhibited a blue shift. The shift in the absorption spectra is in accordance with the Ce^{3+} concentration in the lattice.

Fig. 6. Excitation spectra with emission at 612nm for $Y_2Ce_2O_7$, $Y_{1.9}Ce_2O_7$:*0.1*Eu^{3+} and $Y_2Ce_{1.9}O_7$:*0.1*Eu^{3+} red phosphors. The excitation spectra show intense $^7F_0$-$^5D_2$ (blue) absorption.

Fig. 7. Luminescence emission spectra (excited at 466 nm)for the as prepared samples shows that the PL intensity was found maximum in cerium substituted Eu^{3+} phosphor and is 3.8 times greater than that of the $Ce_{0.9}O_2$:*0.1*Eu^{3+} and $Y_{1.9}Ce_2O_7$:*0.1*Eu^{3+} phosphors.

Fig. 8. Life time decay curves of $^5D_0$-$^7F_2$ transition (wavelength 612 nm) in $Y_{1.9}Ce_2O_7$:*0.1*Eu^{3+} and $Y_2Ce_{1.9}O_7$:*0.1*Eu^{3+} under 466 nm excitation. Decay curves are well fitted with a single exponential decay function $y = Ae^{(-x/t)}$, where "A" is a constant and "t" is the decay time.

Fig. 9. Raman spectra for room-temperature $Y_2Ce_{2-x}O_7$:*x*Eu^{3+} (*x* = 0.05, 0.10, 0.15, 0.20, 0.25 and 0.50) red phosphors. With progressive Eu^{3+} doping the line shape of the allowed modes appears to be broadened.

Fig. 10. Elemental mapping of typical $Y_2Ce_{1.5}O_7$:*0.5*Eu^{3+} red phosphor and it conforms that all the elements are uniformly distributed in the lattice.

Fig. 11. UV-vis absorption spectra of $Y_2Ce_{2-x}O_7$:*x*Eu^{3+} (*x* = 0.05, 0.10, 0.15, 0.20, 0.25 and 0.50) red phosphors.

Fig. 12. Excitation spectra of $Y_2Ce_{2-x}O_7$:*x*Eu^{3+} (*x* = 0.05, 0.10, 0.15, 0.20, 0.25 and 0.50) red phosphors for 612 nm emission. With Eu^{3+} substitution the charge transfer band as well as the intra-4f transitions is also enhanced.

Fig. 13. Emission spectra of $Y_2Ce_{2-x}O_7$:*x*Eu^{3+} (*x* = 0.05, 0.10, 0.15, 0.20, 0.25 and 0.50) red phosphors under 466 nm excitation. As $^5D_0$-$^7F_2$ electric dipole transition intensity dominates over magnetic dipole transition, Eu^{3+} sites have no inversion symmetry. As the Eu^{3+} concentration increases, the asymmetric ratio increases.

Fig. 14. Life time decay curves of $Y_2Ce_{2-x}O_7$:*x*Eu^{3+} (x = 0.05, 0.20, 0.25 and 0.50) under 466 nm excitation.

Fig. 15. Comparison of emission spectra of the commercial red phosphor and $Y_2Ce_{1.5}O_7$:*0.5*Eu^{3+} under 466 nm excitation. It is observed that the red emission intensity of $Y_2Ce_{1.5}O_7$:*0.5*Eu^{3+} is slightly greater than that of commercial red phosphor which clearly demonstrates that the as prepared samples are a promising red phosphor under blue light excitation for white LEDs.

Table 1. Variation of lattice parameter and full width half maximum (FWHM) of 385 cm^{-1} Raman mode of the $Y_2Ce_{2-x}O_7$:xEu^{3+} (x = 0.05, 0.10, 0.15, 0.20, 0.25, 0.50) red phosphors.

x	Lattice parameter (Å)	FWHM of 385 cm^{-1} Raman mode (nm)
0.05	10.775	52.43
0.10	10.7764	70.18
0.15	10.7766	71.12
0.20	10.7784	71.43
0.25	10.7804	75.29
0.50	10.7772	99.21

Table 2. The peak intensity and FWHM of $^5D_0$-$^7F_2$ transition at 612 nm red emission, asymmetric ratio and band gap energy of the as prepared $Y_2Ce_{2-x}O_7$:xEu^{3+} (0.05, 0.10, 0.15, 0.20, 0.25, 0.50) phosphors under 466 nm excitation.

x	Peak Intensity of 612 nm red emission (λ_{exc}= 466 nm) (a.u)	Asymmetric Ratio	FWHM (nm)	Band Gap Energy (E_g) (eV)
0.05	2.2 x 10^5	3.93	4.75	2.93
0.10	3.6 x 10^5	3.96	4.82	2.97
0.15	5.7 x 10^5	4.02	4.89	2.99
0.20	9.9 x 10^5	4.12	4.88	3.01
0.25	1.2 x 10^6	4.39	4.94	3.02
0.50	1.7 x 10^6	4.42	4.93	3.07

Table 3. Spectral parameters, life times and quantum efficiency of $Y_2Ce_{2-x}O_7$:$x$$Eu^{3+}$ (x = 0.05, 0.20, 0.25 and 0.50).

x	J-O intensity Parameters		Transitions	$A_{0\text{-}2,\,4}$ (s^{-1})	A_τ (s^{-1})	τ_{rad} (ms)	β (%)	$\sigma(\lambda_p)$ (pm^2)	τ (ms)	η (%)
	Ω_2 (pm^2)	Ω_4 (pm^2)								
0.05	1.88	0.31	$^5D_0$-$^7F_1$ $^5D_0$-$^7F_2$ $^5D_0$-$^7F_3$	- 105.75 7.98	174.56	5.73	28.6 60.6 4.6	108.86 249.01 722.82	0.618	10.79
0.20	2.06	0.34	$^5D_0$-$^7F_1$ $^5D_0$-$^7F_2$ $^5D_0$-$^7F_3$	- 115.92 8.7	185.88	5.38	26.9 62.4 4.7	141.43 257.17 795.88	0.710	13.20
0.25	2.25	0.36	$^5D_0$-$^7F_1$ $^5D_0$-$^7F_2$ $^5D_0$-$^7F_3$	- 127.49 9.22	199.07	5.02	25.1 64.0 4.6	158.01 274.04 1253.60	0.712	14.08
0.50	2.26	0.36	$^5D_0$-$^7F_1$ $^5D_0$-$^7F_2$ $^5D_0$-$^7F_3$	- 126.82 9.16	196.22	5.10	25.5 64.6 4.7	157.45 276.56 854.72	0.718	14.18

Fig.1.

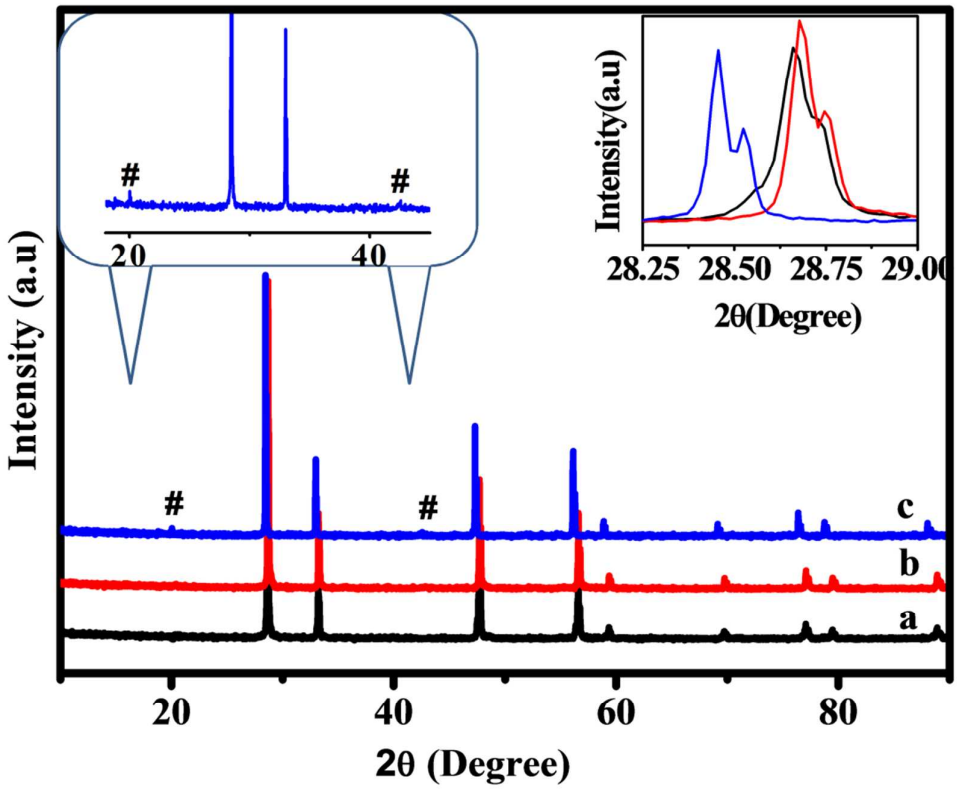

Fig.1. Powder XRD patterns of $Y_2Ce_2O_7$, $Y_{1.9}Ce_2O_7$:*0.1*Eu^{3+} and $Y_2Ce_{1.9}O_7$:*0.1*Eu^{3+} phosphors. For $Y_2Ce_{1.9}O_7$:*0.1*Eu^{3+}additional cubic C-type peaks (denoted by #) appear in the XRD pattern (inset). The inset Fig. shows the expanded view of the peak around 2θ 28-29°.

Fig.2

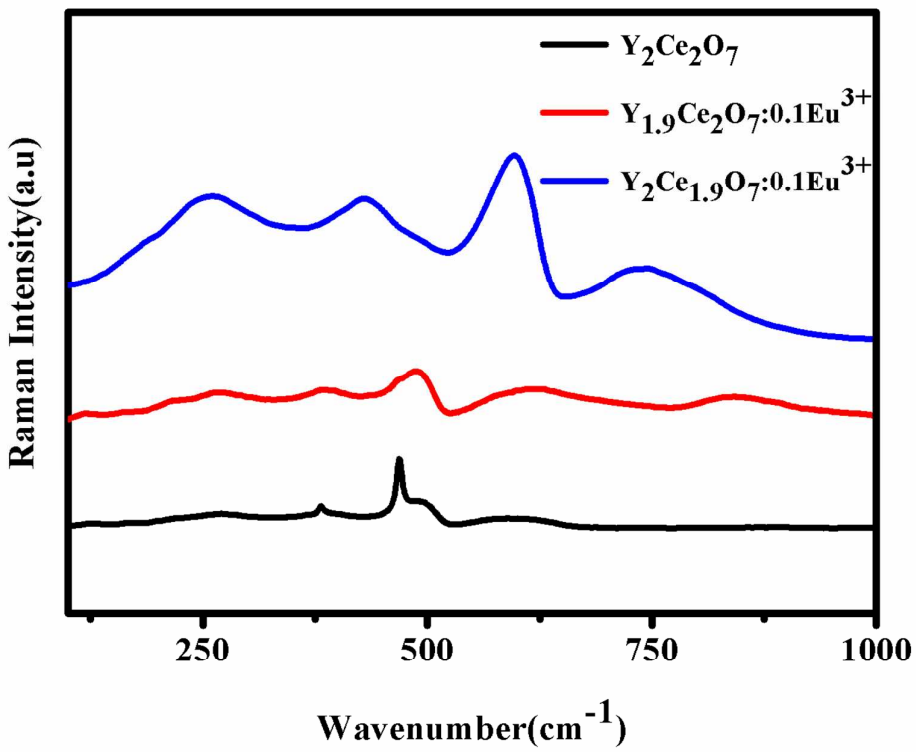

Fig. 2. Raman spectra of $Y_2Ce_2O_7$, $Y_{1.9}Ce_2O_7$:*0.1*Eu^{3+} and $Y_2Ce_{1.9}O_7$:*0.1*Eu^{3+}phosphors.

Fig.3.

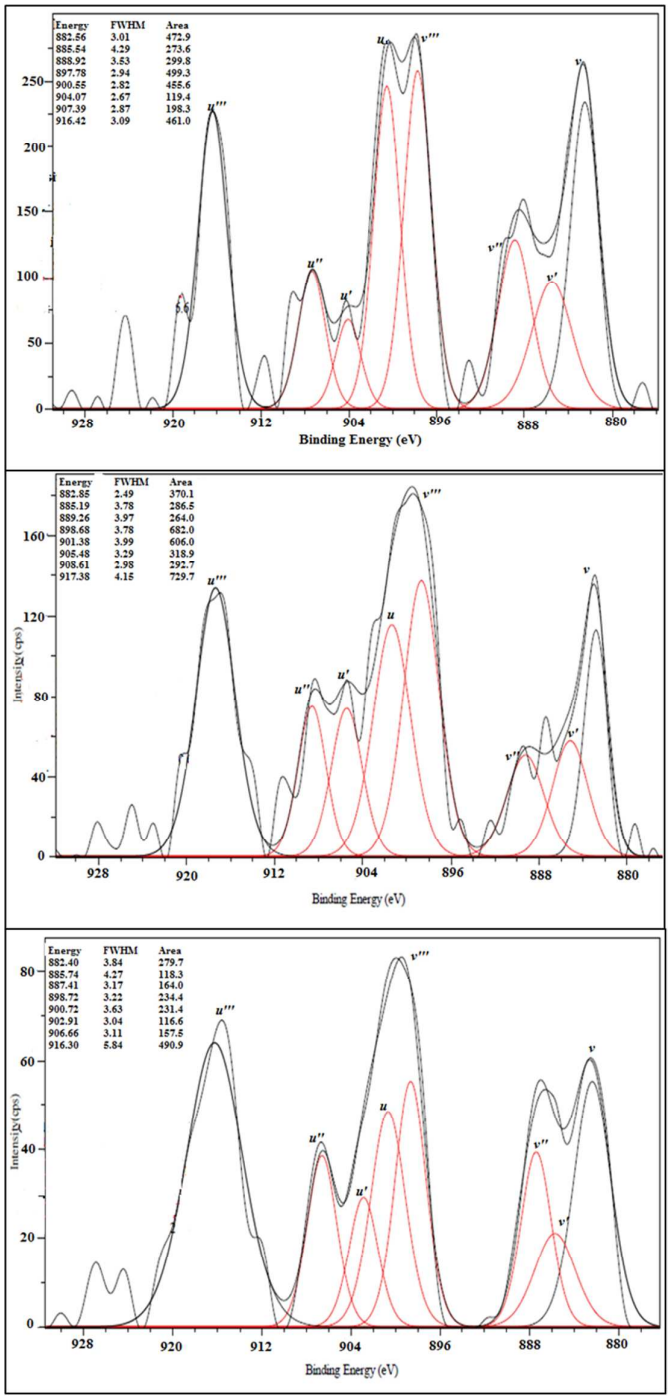

Fig. 3. XPS spectrum of Ce(3d) for the $Y_2Ce_2O_7$,$Y_{1.9}Ce_2O_7$:*0.1*Eu^{3+} and $Y_2Ce_{1.9}O_7$:*0.1*Eu^{3+} phosphors was deconvoluted to give the individual spin-orbit doublet of $3d_{3/2}$ and $3d_{5/2}$, and the sum of the deconvoluted peaks was used to produce the fit to the actual data.

Fig.4.

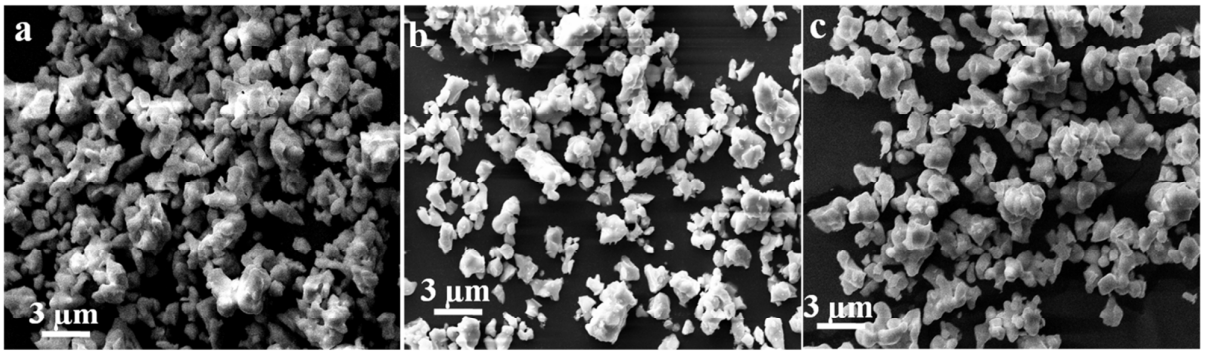

Fig. 4. Typical SEM photographs of a) $Y_2Ce_2O_7$, b) $Y_{1.9}Ce_2O_7$:*0.1*Eu^{3+} and c) $Y_2Ce_{1.9}O_7$:*0.1*Eu^{3+} phosphors. The particles are slightly agglomerated and there is a broad distribution of particle size with an average size of 1-3 µm.

Fig.5.

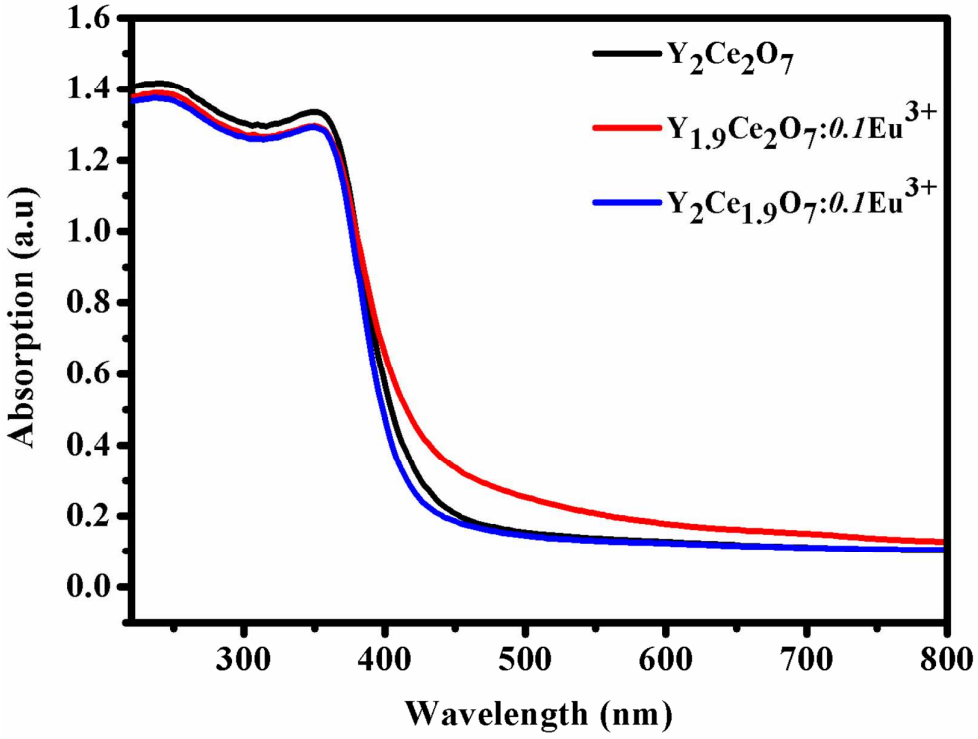

Fig. 5. UV-vis absorption spectra of $Y_2Ce_2O_7$, $Y_{1.9}Ce_2O_7$:*0.1*Eu^{3+} and $Y_2Ce_{1.9}O_7$:*0.1*Eu^{3+} phosphors. The absorption spectra of $Y_{1.9}Ce_2O_7$:*0.1*Eu^{3+} phosphor exhibited a red shift compared with that of the host $Y_2Ce_2O_7$ while $Y_2Ce_{1.9}O_7$:*0.1*Eu^{3+} phosphors exhibited a blue shift. The shift in the absorption spectra is in accordance with the Ce^{3+} concentration in the lattice.

Fig.6.

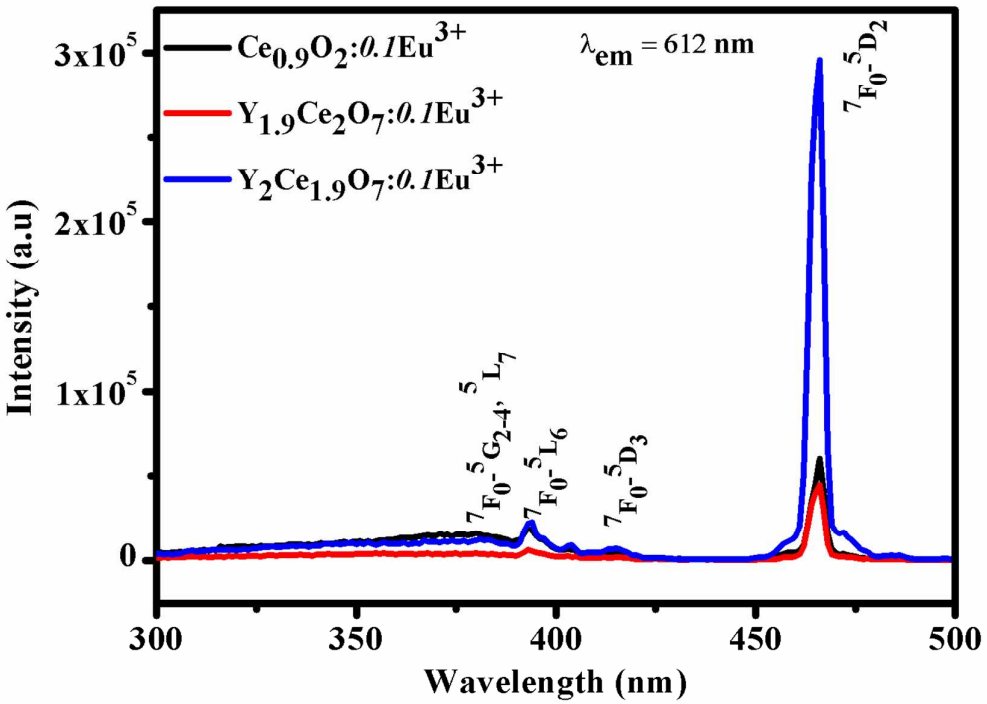

Fig. 6. Excitation spectra with emission at 612nm for $Y_2Ce_2O_7$, $Y_{1.9}Ce_2O_7$:*0.1*Eu^{3+} and $Y_2Ce_{1.9}O_7$:*0.1*Eu^{3+} red phosphors. The excitation spectra show intense $^7F_0$-$^5D_2$ (blue) absorption.

Fig.7.

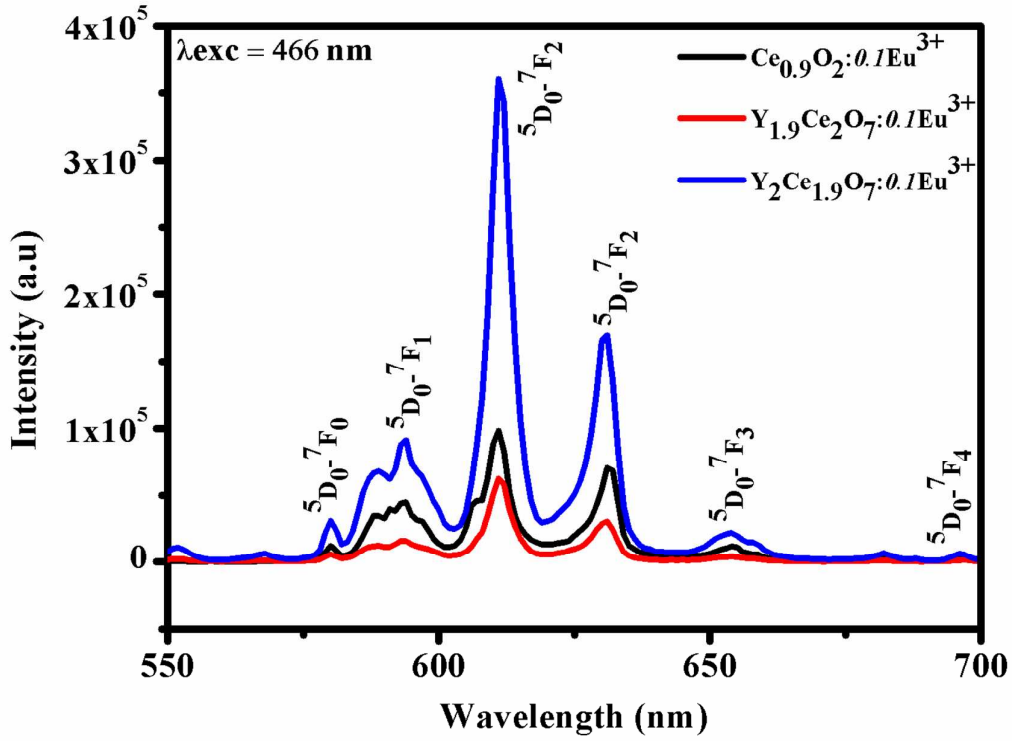

Fig. 7. Luminescence emission spectra (excited at 466 nm) for the as prepared samples shows that the PL intensity was found maximum in cerium substituted Eu^{3+} phosphor and is 3.8 times greater than that of the $Ce_{0.9}O_2$:*0.1*Eu^{3+} and $Y_{1.9}Ce_2O_7$:*0.1*Eu^{3+} phosphors.

Fig.8.

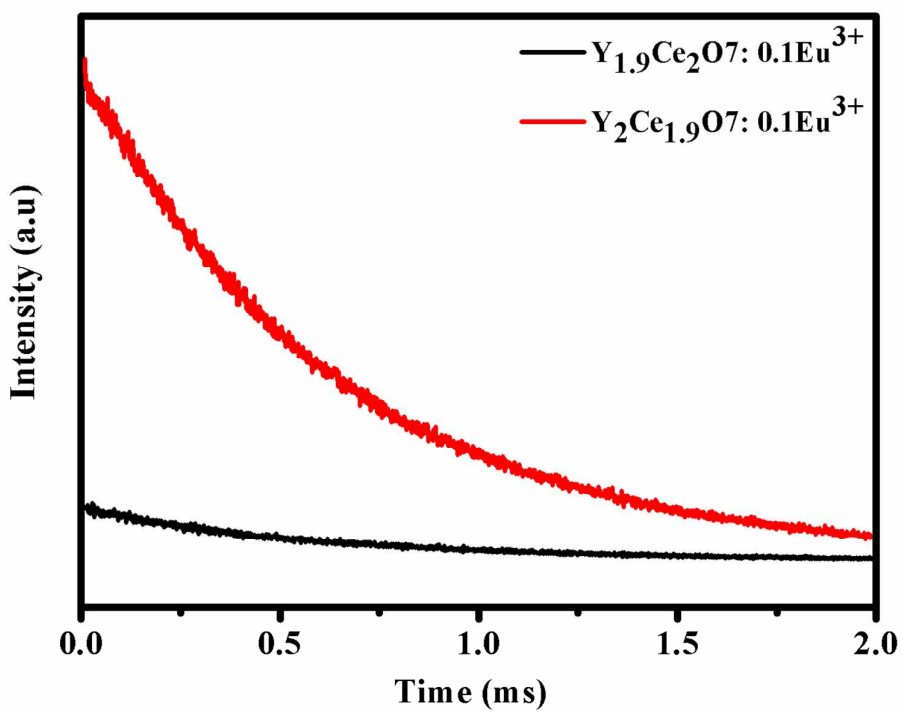

Fig. 8. Life time decay curves of $^5D_0$-$^7F_2$ transition (wavelength 612 nm) in $Y_{1.9}Ce_2O_7$:*0.1*Eu^{3+} and $Y_2Ce_{1.9}O_7$:*0.1*Eu^{3+} under 466 nm excitation. Decay curves are well fitted with a single exponential decay function $y = Ae^{(-x/t)}$, where "A" is a constant and "t" is the decay time.

Fig.9.

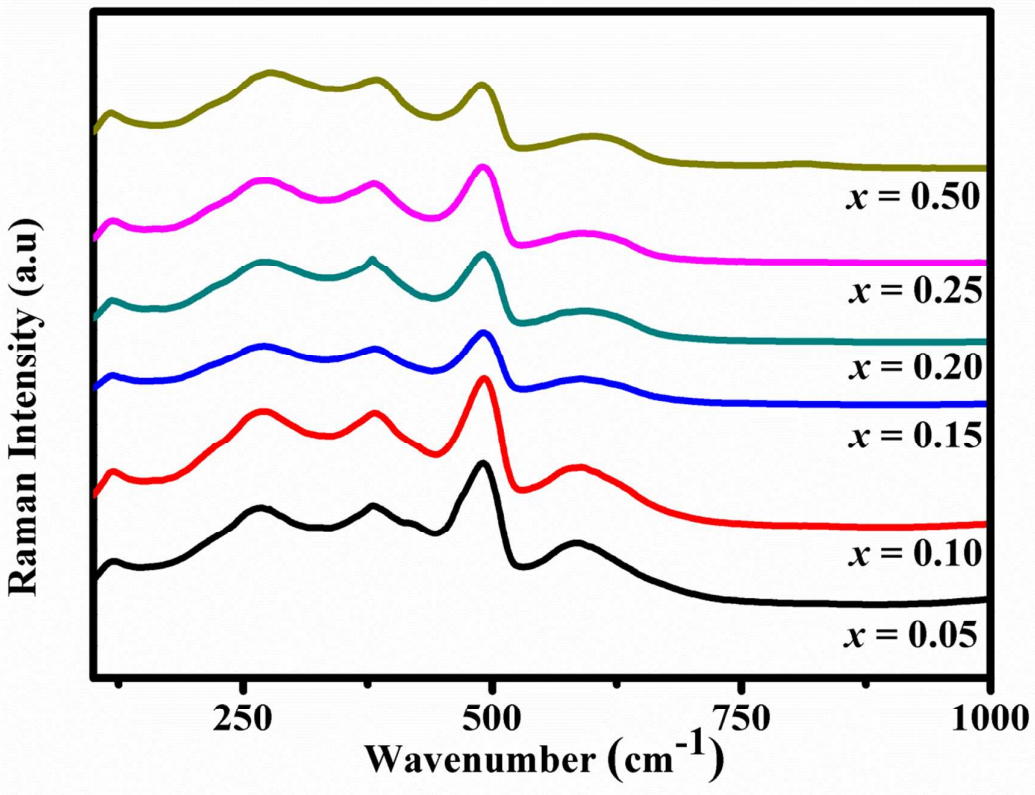

Fig. 9. Raman spectra for room-temperature $Y_2Ce_{2-x}O_7$:xEu^{3+} (x = 0.05, 0.10, 0.15, 0.20, 0.25 and 0.50) red phosphors. With progressive Eu^{3+} doping the line shape of the allowed modes appears to be broadened.

Fig.10.

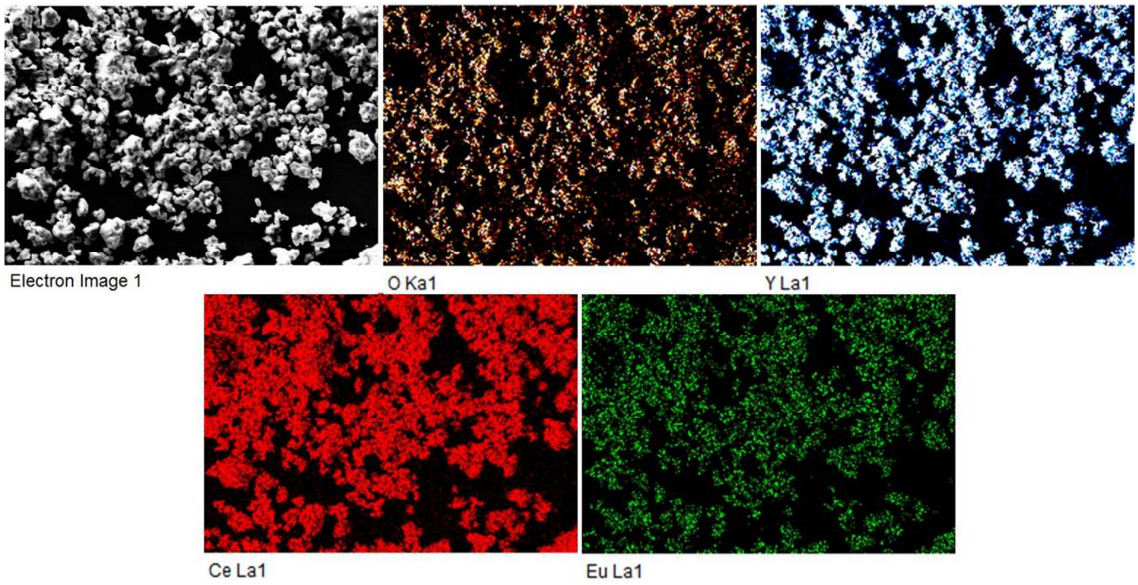

Fig. 10. Elemental mapping of typical $Y_2Ce_{1.5}O_7$:*0.5*Eu^{3+} red phosphor and it conforms that all the elements are uniformly distributed in the lattice.

Fig.11.

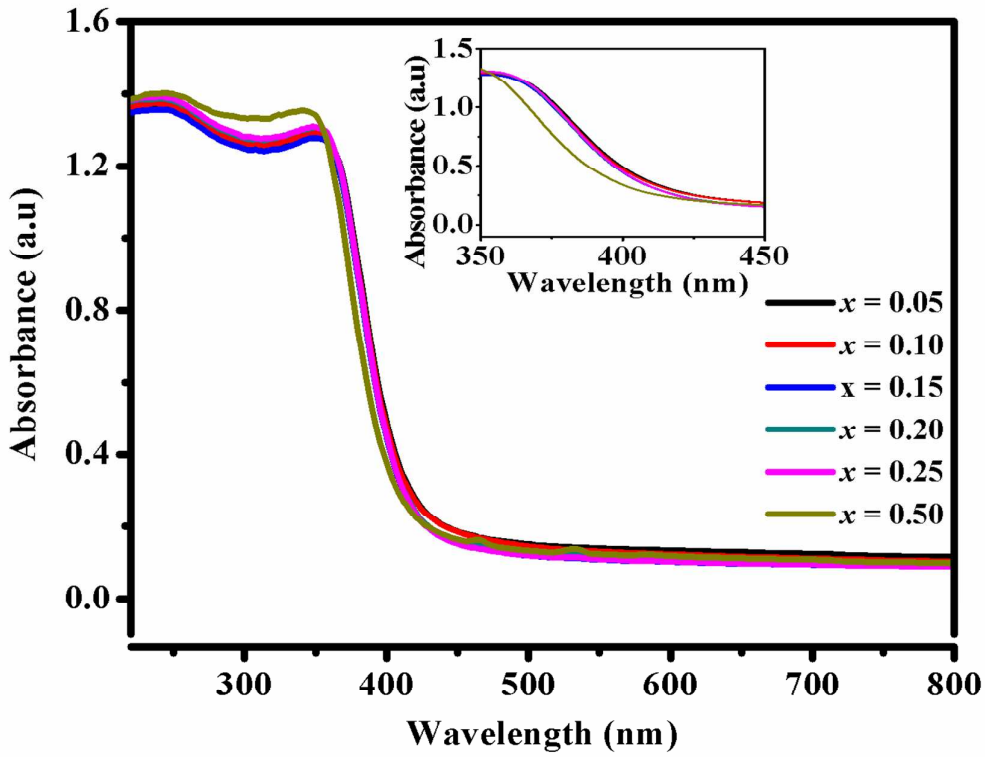

Fig. 11. UV-vis absorption spectra of $Y_2Ce_{2-x}O_7:xEu^{3+}$ (x = 0.05, 0.10, 0.15, 0.20, 0.25 and 0.50) red phosphors.

Fig. 12.

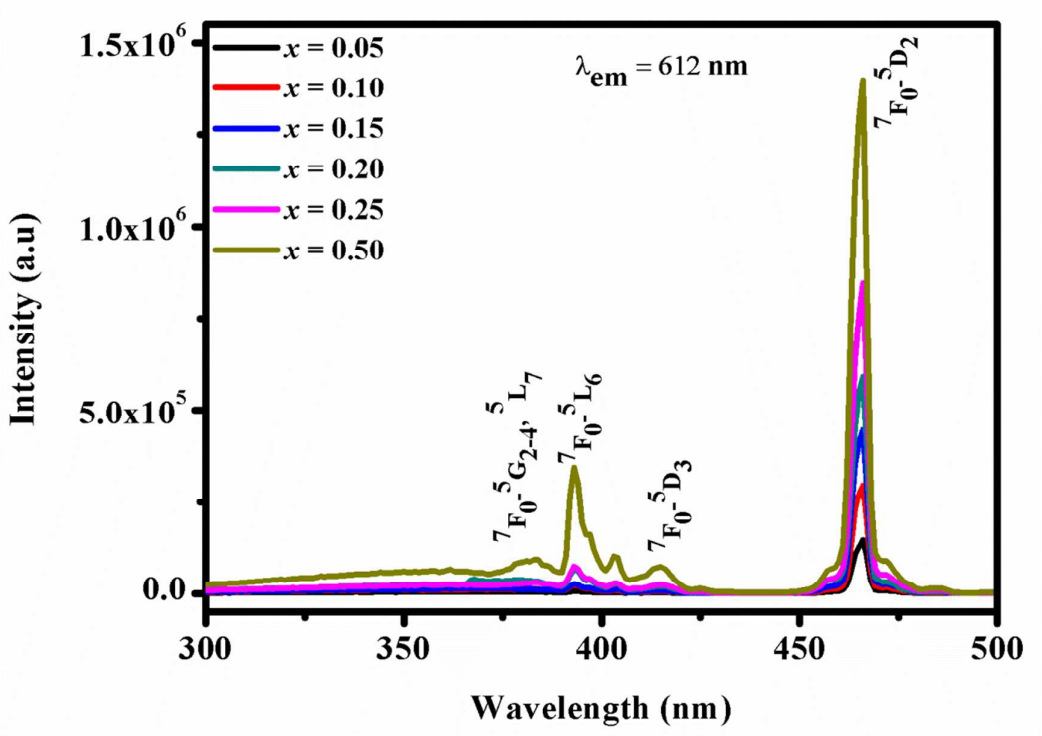

Fig. 12. Excitation spectra of $Y_2Ce_{2-x}O_7$:xEu^{3+} (x = 0.05, 0.10, 0.15, 0.20, 0.25 and 0.50) red phosphors for 612 nm emission. With Eu^{3+} substitution the charge transfer band as well as the intra-4f transitions is also enhanced.

Fig. 13.

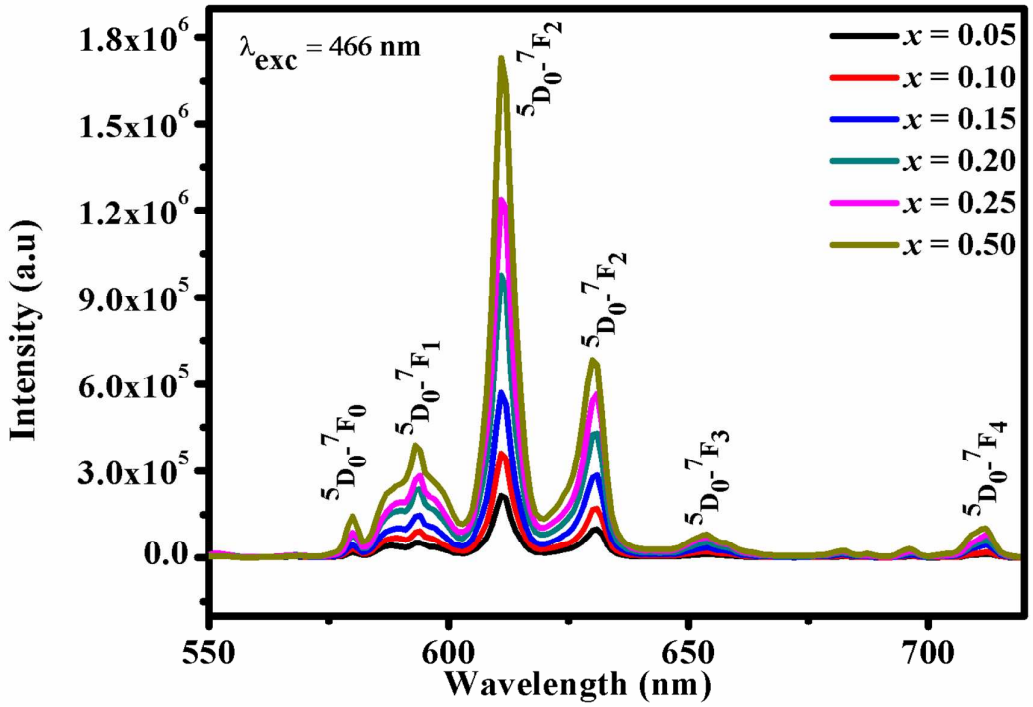

Fig. 13. Emission spectra of $Y_2Ce_{2-x}O_7$:xEu^{3+} (x = 0.05, 0.10, 0.15, 0.20, 0.25 and 0.50) red phosphors under 466 nm excitation. As $^5D_0$-$^7F_2$ electric dipole transition intensity dominates over magnetic dipole transition, Eu^{3+} sites have no inversion symmetry. As the Eu^{3+} concentration increases, the asymmetric ratio increases.

Fig.14.

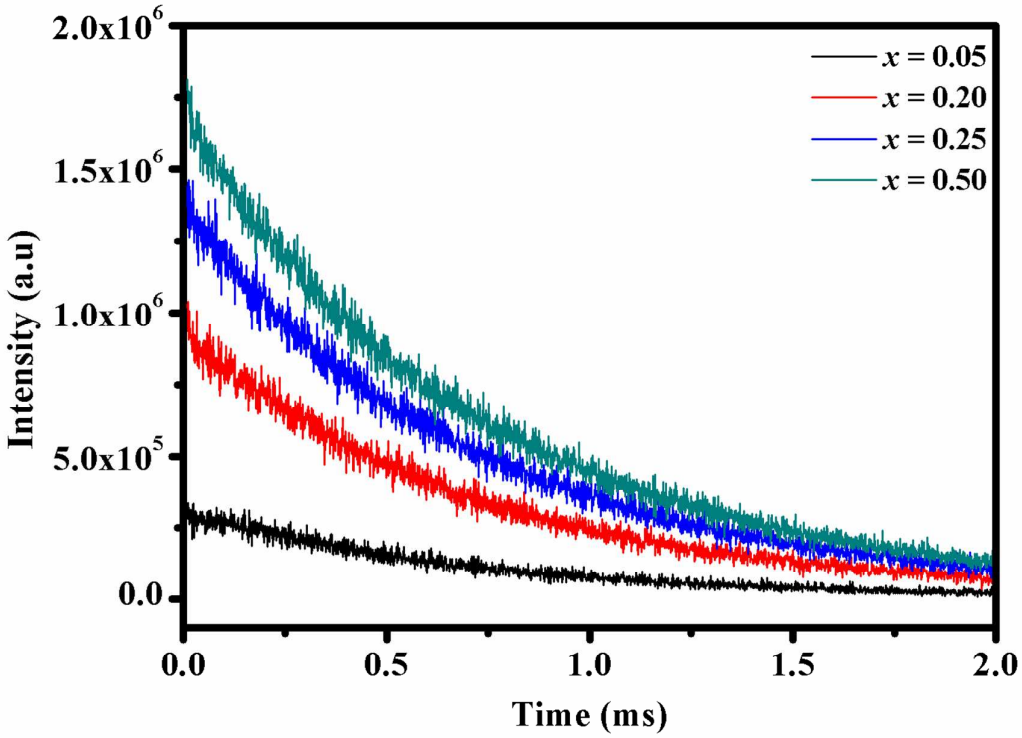

Fig. 14. Life time decay curves of $Y_2Ce_{2-x}O_7$:xEu^{3+} (x = 0.05, 0.20, 0.25 and 0.50) under 466 nm excitation.

Fig.15.

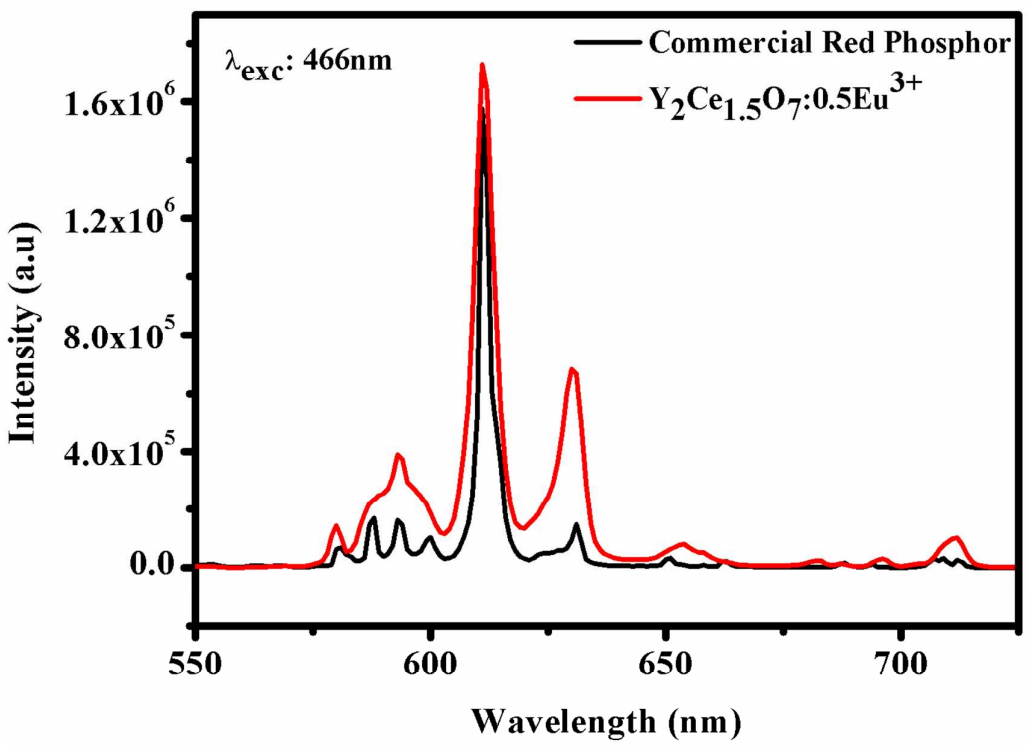

Fig. 15. Comparison of emission spectra of the commercial red phosphor and $Y_2Ce_{1.5}O_7$:*0.5*Eu^{3+} under 466 nmexcitation. It is observed that the red emission intensity of $Y_2Ce_{1.5}O_7$:*0.5*Eu^{3+} is slightly greater than that of commercial red phosphor which clearly demonstrates that the as prepared samples are a promising red phosphor under blue light excitation for white LEDs.